Journal of the Taiwan Institute of Chemical Engineers 64 (2016) 79–88

Contents lists available at ScienceDirect

Journal of the Taiwan Institute of Chemical Engineers

journal homepage: www.elsevier.com/locate/jtice

Sphere-like Mn_2O_3 nanoparticles: Facile hydrothermal synthesis and adsorption properties

Mostafa Y. Nassar*, Alaa S. Amin, Ibrahim S. Ahmed, Samar Abdallah

Chemistry Department, Faculty of Science, Benha University, Benha 13518, Egypt

ARTICLE INFO

Article history:
Received 6 October 2015
Revised 1 February 2016
Accepted 22 March 2016
Available online 12 April 2016

Keywords:
Hydrothermal synthesis
Ammonium carbonate
Manganese carbonate
Mn_2O_3 nanostructures
Reactive Black 5 dye
Adsorption properties

ABSTRACT

Thermal decomposition of the hydrothermally prepared $MnCO_3$ produced pure Mn_2O_3 nanoparticles with 23 nm crystallite size. The products were characterized and the adsorption properties of Mn_2O_3 adsorbent were investigated using Reactive Black 5 dye. Thence, some factors affecting the adsorption process were studied and the results exhibited good adsorption capacity ($q_m = 14.6$ mg/g) of the adsorbent and the percent dye removal reached 92% in 40 min. Additionally, the kinetics, thermodynamics, and isotherms of the adsorption were investigated. The Langmuir model fitted the adsorption data. The adsorption process followed pseudo-second-order kinetic model. The adsorption of the dye on Mn_2O_3 adsorbent is an endothermic ($\Delta H^o = 44.52$ kJ/mol) and spontaneous ($\Delta G^o = -21.63$ kJ/mol) process.

1. Introduction

Recently, water pollution has received a great attention because it is one of the main environmental threats to our life due to the imbalance and significant changes in the hydrological cycle that cause many health difficulties [1–7]. Approximately, 1–20% of organic dyes are discharged, after their use in dye-including industries, into the environment and they pollute huge quantities of water [8]. Organic pollutants are also produced from various sources such as paper, leather, plastics, pulp, refineries, and chemical industries [9]. Among these dyes is Reactive Black 5 dye and since this dye has one azoic bond (−N=N−) in its structure, it is carcinogenic and toxic [10,11]. Moreover, such dye-polluted wastewater not only results in eye burn, but also causes many problematic issues to aquatic life. Therefore, removal of the textile dyes from wastewaters is an essential aspect and has drawn interest of many research groups [12–14]. In such, various physical and chemical methods; such as sedimentation, coagulation, reverse osmosis, ultrasonication, ozonation, membrane separation, photocatalysis, adsorption, ion exchange, *etc*., have been exploited for treatment of wastewater [13–18]. However, adsorption process is the most essential technique in organic dye removal from wastewater and it is still more environmentally and economically preferable over the other techniques. Searching for inexpensive, environmentally friendly, and efficient adsorbents is a big challenge. Therefore, various adsorbents such as agricultural wastes, activated carbons, sesame hulls, biochars, clay materials, and organic resins have been suggested by different research groups [19–23].

Based on large numbers of active sites and high surface area of the material nanostructures, researchers have devoted their interest to fabricate different nanosized metal oxides and nanocomposites using various routes and suggested them as adsorbents [24–27]. Nanosized manganese oxides and their composites have received a considerable interest because of nontoxicity, and various applications such as catalysis, adsorption, ion exchange, electrochemical storage and biosensor [28–33]. However, due to low cost and practical view point, Mn_2O_3 nanostructures have received a great attention. Various Mn_2O_3 nanostructures have been synthesized using several methods such as hydrothermal, precipitation, solid-state reaction, and sol–gel method [34–37]. Additionally, many Mn_2O_3 morphologies; rod, octahedral, cube, and wire-like have been prepared [38–40]. The hydrothermal process is more preferable over the other synthesis techniques owing to the several advantages that this technique has such as simplicity and the availability of tuning several parameters to control the crystallite size and the morphological form of the nanostructure products [41–43]. It is noteworthy that the hydrothermal synthesis of metal carbonates and their thermal conversion into the corresponding metal oxide nanoparticles have recently attracted much attention because the release of CO_2 gas during the thermal decomposition step results in formation of nanopores in the

* Corresponding author. Tel.: +20 1068727555; fax: +20 133222578.
E-mail address: m_y_nassar@yahoo.com, m_y_nassar@fsc.bu.eg.edu, mostafaynassar@gmail.com (M.Y. Nassar).

http://dx.doi.org/10.1016/j.jtice.2016.03.041
1876-1070/

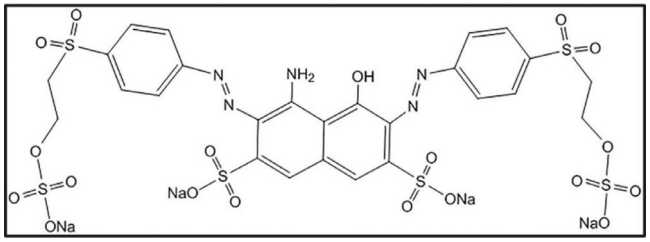

Scheme. 1. Chemical structure of Reactive Black 5 dye.

products and this, in turn, helps to produce new nanostructures with high surface area [44,45]. However, to the best of our knowledge, hydrothermal preparation of uniform $MnCO_3$ microspheres smaller than 1 μm is a big challenge and their thermal decomposition to produce Mn_2O_3 nanoparticles are rarely published [46,47].

Herein, in continuation of our recent work, a simple approach was conducted, for the first time, to synthesize pure uniform microspheres of $MnCO_3$ in a high yield via a template-free hydrothermal treatment of manganese chloride and ammonium hydrogen carbonate. Thermal decomposition of the as-prepared $MnCO_3$ produced pure phase of Mn_2O_3 nanoparticles and the as-synthesized products were identified using XRD, FE-SEM, TG, HR-TEM and FT-IR. Moreover, removal of the Reactive Black 5 dye (RB5) pollutant, Scheme 1, from aqueous solutions using the as-prepared Mn_2O_3 as an adsorbent was investigated by evaluation of its adsorption properties, adsorption kinetics, and isotherms under varied conditions; contact time, pH, ionic strength, and temperature.

2. Materials and methods

2.1. Materials

Manganese chloride ($MnCl_2.4H_2O$) was purchased from Sigma–Aldrich company, ammonium hydrogen carbonate (NH_4HCO_3) was supplied by Fluka company, and Reactive Black 5 dye (RB5) ($C_{26}H_{21}N_5Na_4O_{19}S_6$) was purchased from Huntsman International (India) Private Limited, India. Hydrochloric acid, sodium hydroxide (pellets), potassium chloride, and ethanol were purchased from El-Nasr pharmaceutical chemicals company (analytical reagent grade, Egypt). All chemicals were used as supplied without further purification.

2.2. Preparation of $MnCO_3$ and Mn_2O_3 nanoparticles

In a typical hydrothermal treatment: an aqueous solution of ammonium hydrogen carbonates (4.95 g, 62.6 mmol, 3 eq.) (30 mL) was added to a stirring aqueous solution of manganese chloride (4.13 g, 20.9 mmol, 1 eq.) (30 mL). The stirring was allowed to continue for 10 min. Afterwards, the produced reaction blend was placed in a Teflon-lined stainless steel autoclave (capacity 100 mL) and the autoclave was then heated at 80 °C for 30 min in an electric oven. The autoclave was allowed to get the room temperature naturally. The produced precipitate ($MnCO_3$) was collected by centrifugation, washed several times with distilled water and then with ethanol and finally dried at *ca.* 60 °C overnight.

Mn_2O_3 nanoparticles were produced by heating the as-prepared manganese (II) carbonate ($MnCO_3$) at 550 °C for 1 h in air.

2.3. Characterization

The X-ray diffractometer (Bruker; model D8 Advance) with monochromated Cu-Kα radiation ($\lambda = 1.54178$ Å) was used to identify the crystallinity and phase purity of the as-prepared products. FE-SEM pictures were collected on a field emission scanning electron microscope (FE-SEM) connected with a microscope (JEOL JSM-6500F). The morphology and particle size of the product were examined using a high resolution transmission electron microscope (HR-TEM) (JEM-2100) with 200 kV accelerating voltage. Using an FT-IR spectrometer (Thermo Scientific; model Nicolet iS10) from 4000 to 400 cm^{-1}, the FT-IR spectra were performed. On a Jasco UV–Visible spectrophotometer (Jasco; model v670), the UV–Visible spectra of the RB5 dye were measured in the adsorption investigation. The thermal gravimetric analysis (TG) of the as-prepared manganese carbonate was carried out by means of a thermal analyzer instrument (Shimadzu; model TA-60WS) with 15 °C/min heating rate, under N_2 gas atmosphere.

2.4. Adsorption studies

The batch adsorption experiments were conducted under magnetic stirring in 100-mL Erlenmeyer flasks using a Reactive Black 5 dye (RB5) as an example for textile industry pollutants. Various experimental parameters influencing the RB5 dye adsorption including contact time (10–70 min), initial pH (1– 9) of the dye solution, initial concentration (10–50 mg/L), ionic strength, and temperature (298–318 K) were examined. In the adsorption experiments, pH value of RB5 dye aqueous solution (25 mL) of a desired concentration was adjusted by using 0.1 M HCl or NaOH aqueous solutions. Thereafter, a certain amount (0.05 g) of the as-prepared Mn_2O_3 nanoparticles was added and magnetically stirred (400 rpm) for a designated time period at a certain temperature. Based on the factors under study, the dye temperatures and concentrations were changed. After stirring for a specific time, an aliquot was withdrawn from the flask, the mixture was centrifuged at 4000 rpm to separate the adsorbent and then the remaining concentration of the RB5 dye was measured in the supernatant solution using a UV–Vis spectrophotometer. The adsorption experiments were performed three times and average values were taken. Notably, the dye concentration was determined using a previously constructed calibration plot. By having the initial dye concentration (C_0; mg/L), remaining dye concentration (C_t; mg/L) at time t, dye solution volume (V; L), and mass of Mn_2O_3 nanomaterial (m; g), the adsorption capacity (q_t; mg/g) and the dye removal efficiency (% R), can be calculated using Eqs. (1) and (2).

$$q_t = \frac{V(C_0 - C_t)}{\mathrm{m}} \quad (1)$$

$$\%\ \mathrm{R} = \frac{(C_0 - C_t)}{C_0} \times 100 \quad (2)$$

3. Results and discussion

3.1. Structural, thermal and morphological studies

A facile hydrothermal treatment of aqueous solutions of manganese chloride and ammonium hydrogen carbonate with a molar ratio of 1:3, respectively, at 80 °C for only 30 min has been examined in the absence of template agents and unfriendly organic solvents. Also, the as-prepared $MnCO_3$ precursor was then thermally converted into Mn_2O_3 nanoparticles as will shortly be discussed. The as-synthesized manganese carbonate precursor and the product have been identified using various spectroscopic techniques.

3.1.1. XRD analysis

The crystal structures of the as-prepared $MnCO_3$ and Mn_2O_3 have been studied by X-ray diffraction (XRD) spectroscopy. Fig. 1a shows the XRD pattern of the $MnCO_3$ precursor prepared using the aforementioned hydrothermal treatment. All reflections are readily indexed to pure hexagonal phase structure of rhodochrosite manganese carbonate ($MnCO_3$) which is in complete agreement with

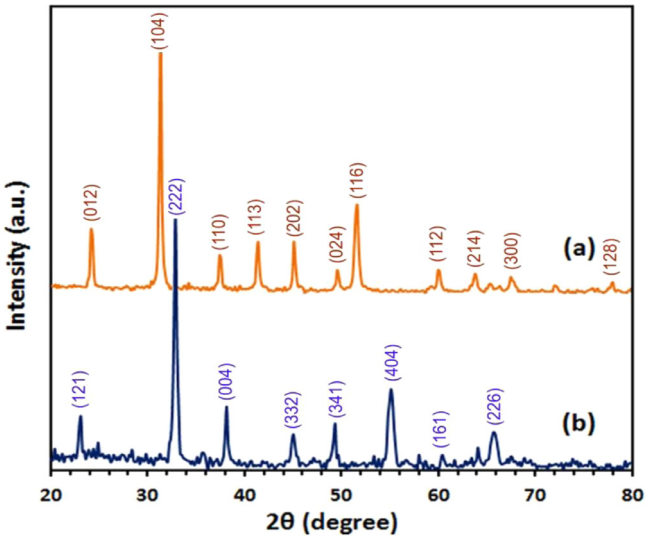

Fig. 1. (a,b). XRD patterns of the as-prepared $MnCO_3$ (a), and Mn_2O_3 (b).

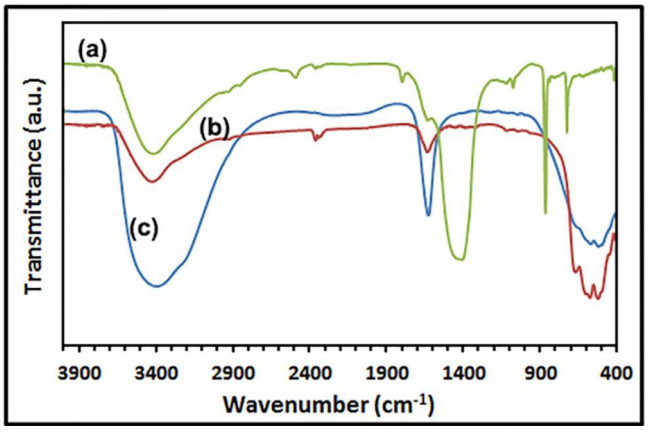

Fig. 2. FT-IR spectra of the as-prepared $MnCO_3$ (a), Mn_2O_3 (b), and RB5 loaded Mn_2O_3 (c).

the standard patterns of $MnCO_3$ (space group R-3c, JCPDS card 44-1472) [31]. Other characteristic reflections related to any impurities have not been seen. By knowing the wavelength of the X-ray (λ), the full width of the reflection at half maximum (β), and the Bragg diffraction angle (θ_B), and applying them in the Debye–Scherrer equation (Eq. 3), the average crystallite size (D) of the as-synthesized $MnCO_3$ was estimated to be 42 nm [48].

$$D = 0.9\lambda/\beta\cos\theta_B \quad (3)$$

Fig. 1b presents the X-ray diffraction pattern of Mn_2O_3 nanoparticles obtained by thermal decomposition of the as-synthesized $MnCO_3$ at 550 °C for 1 h in air. The XRD pattern matches well and can be readily indexed to orthorhombic Mn_2O_3 (space group P21/c, JCPDS card 73-1826) [49]. No other characteristic reflections of any impurities have been observed. The calculated mean average crystallite size of the as-produced Mn_2O_3 particles using the Debye–Scherrer Eq. (3) was found to be 23 nm.

3.1.2. FT-IR analysis

The chemical structure and bonding of both manganese carbonate ($MnCO_3$) and manganese sequioxide (Mn_2O_3) have also been studied using the FT-IR spectroscopy. Fig. 2(a,b) displays the FT-IR spectra of the as-prepared $MnCO_3$ and Mn_2O_3, respectively. The FT-IR spectrum of the $MnCO_3$, Fig. 2(a), confirms the presence of carbonate anions in the manganese carbonate by

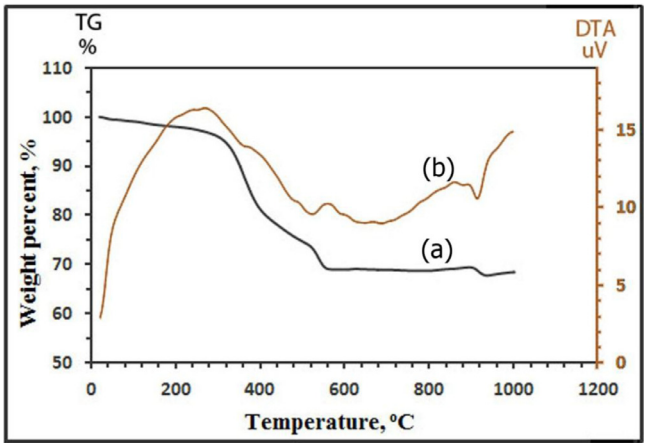

Fig. 3. (a,b). TG (a) and DTA (b) analyses of the as-prepared $MnCO_3$ under N_2 gas.

revealing the D_{3h} symmetry fingerprint peaks centered at 723, 862, and 1387 cm^{-1} which are attributed to $\nu_4(E''')$, $\nu_2(A_2'')$, and $\nu_3(E')$ vibrational modes, respectively, corresponding to the reported vibration normal modes of planar XO_3 molecules or ions (X = C atom, in our case) [50]. The shoulder centered at *ca.* 1748 cm^{-1} may be ascribed to a combination of some vibrations of CO_3^{2-} anions and divalent metal ions [25]. Plus, the band exhibited at 2472 cm^{-1} can also be assigned to the vibrational mode of the CO_3^{2-}anions [50]. However, the as-synthesized precursor features one shoulder at 1584 cm^{-1} and one strong peak at 3372 cm^{-1} which may be due to the O–H bending and stretching vibrations of water molecules, respectively, adsorbed on the $MnCO_3$ surface [24,44]. On the other hand, inspection of the FT-IR spectrum of the as-produced Mn_2O_3, Fig. 2(b), reveals disappearance of the characteristic peaks of $MnCO_3$ and appearance of three peaks instead at 491, 560, and 633 cm^{-1} which can be ascribed to Mn–O stretching vibrations [51]. Also, Fig. 2(b) evinces two vibrational bands at 1602 and 3372 cm^{-1} corresponding to bending and stretching vibrations, respectively, of the adsorbed surface water molecules on the Mn_2O_3 nanoparticles [52].

3.1.3. Thermal analysis

The TG/DTA analyses of the as-synthesized $MnCO_3$ were investigated and presented in Fig. 3(a,b), respectively. The TG curve, Fig. 3a, reveals three mass loss steps, With an overall mass loss of 32.50%, for the thermal decomposition of the $MnCO_3$ sample under N_2 atmosphere. The first mass loss appeared in the temperature range 60–250 °C may be due to the loss of the adsorbed water molecules, 1.60% (calc. 1.54%). Upon increasing the temperature, $MnCO_3$ sample was decomposed and gave off CO_2 and CO gases to produce Mn_2O_3 and this was indicated by observing two close steps overlapped into almost one significant weight loss step in the temperature range 250–550 °C, 30.9% (calc. 30.84%). The produced Mn_2O_3, 67.5% (calc. 67.62%). is stable till temperature 900 °C, and increasing the temperature over 900 °C converts Mn_2O_3 to Mn_3O_4 and this observation is consistent well with the reported data [53,54]. On the other hand, DTA thermal analysis of the $MnCO_3$ sample exhibited three endothermic peaks attributed to the desorption of the adsorbed water, thermal decomposition of $MnCO_3$ producing Mn_2O_3, and conversion of Mn_2O_3 to Mn_3O_4, respectively, as depicted in Fig. 3(b).

3.1.4. Morphological studies

The microstructures of the as-prepared products and their morphologies have been examined using FE-SEM and HR-TEM, as presented in Figs. 4 and 5, respectively. Fig. 4(a) presents a low magnification FE-SEM image of the as-synthesized $MnCO_3$ and this

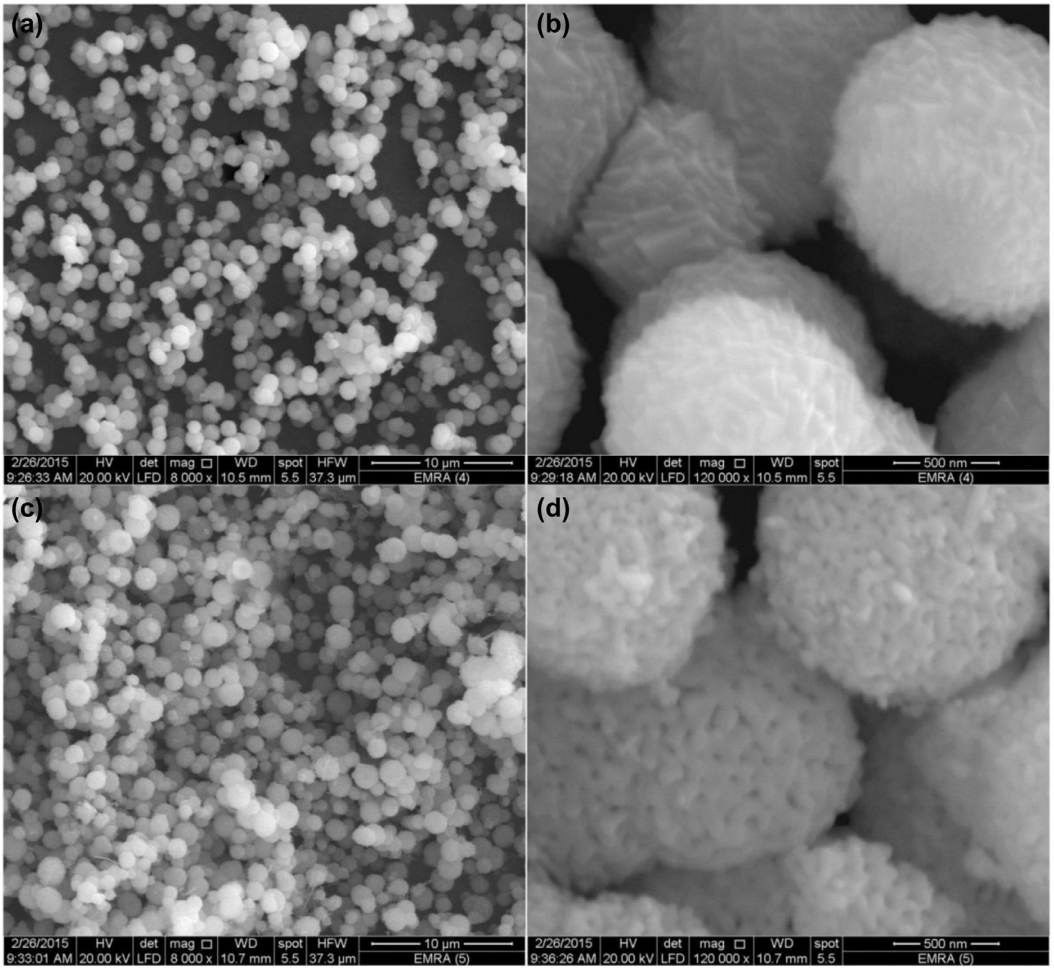

Fig. 4. (a–d). FE-SEM images for the as-prepared $MnCO_3$ (a,b), and Mn_2O_3 (c,d); low (a,c) and high (b,d) magnification images.

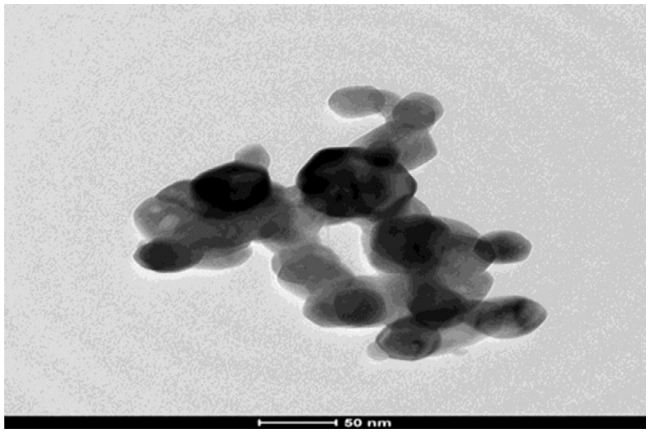

Fig. 5. HR-TEM image for the as-prepared Mn_2O_3 nanoparticles.

image reveals a uniform spherical morphology of $MnCO_3$ with an average diameter of *ca.* 1.5 μm. However, a close inspection of the highly magnified FE-SEM image of $MnCO_3$, Fig. 4(b), reveals that the surfaces of the $MnCO_3$ spheres are composed of nano-cubic shaped particles with an average size of about 82 nm. Plus, there are some voids inside the surfaces indicating the presence of the hierarchical hollow structure. Interestingly, this morphology has not been changed on calcination to produce Mn_2O_3, *i.e.* uniform microspheres with a diameter of *ca.* 1.5 μm and their spheres are composed of tiny cubic shaped particles with a diameter of about 85 nm, as shown in Fig. 4(c,d), for the low and high magnification FE-SEM images, respectively. The obtained spherical morphologies for both $MnCO_3$ and Mn_2O_3 in our case are smaller and different from the cubic morphology reported ones [31,55] and they also are significantly smaller in size than the similarly reported morphology [47]. Moreover, investigation of the microstructures of the as-produced Mn_2O_3 nanoparticles using HR-TEM, Fig. 5, exhibits that Mn_2O_3 nanoparticles consisted of hexagonal and cubic like particles with an average size of 25 nm which is consistent with the size estimated from the XRD data.

3.2. Adsorption studies on Mn_2O_3 nanoparticles

Utilizing the as-prepared Mn_2O_3 nanoparticles as an adsorbent was investigated using Reactive Black 5 dye (RB5) as an adsorbate and a textile industry pollutant, as well. The adsorption can be confirmed by investigating the FT-IR spectra of the adsorbent, before and after the adsorption process, as reported by Khan and others [19,56]. The FT-IR spectrum of Mn_2O_3 after RB5 dye adsorption (Fig. 2c) revealed a noticeable change in some peaks; the peaks appeared at 3372 and 1602 cm^{-1} (Fig. 2b) due to O–H stretching and bending vibrations of the adsorbed surface water molecules, for Mn_2O_3 nanoparticles, were shifted after adsorption to 3357 and 1614 cm^{-1} (Fig. 2c), respectively, and their intensities were also significantly increased. The latter two peaks can be attributed to stretching and bending vibrations of the OH group of the adsorbed RB5 dye molecules on the Mn_2O_3 adsorbent, and these results are

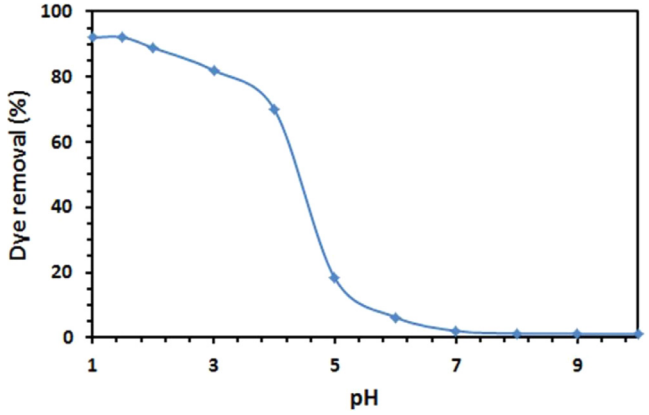

Fig. 6. pH influence on RB5 dye removal percentage.

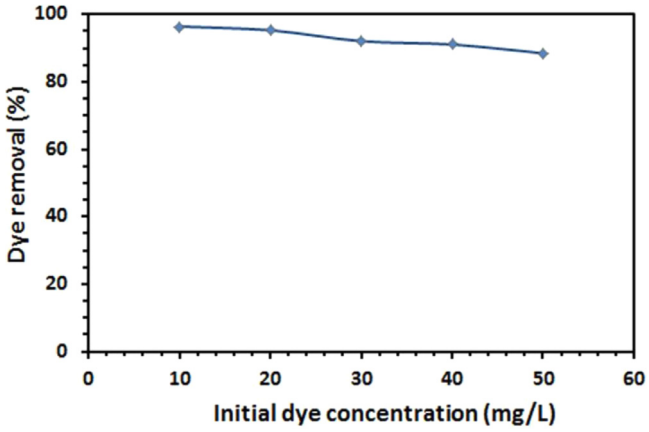

Fig. 7. Influence of initial dye concentration on RB5 dye removal percentage.

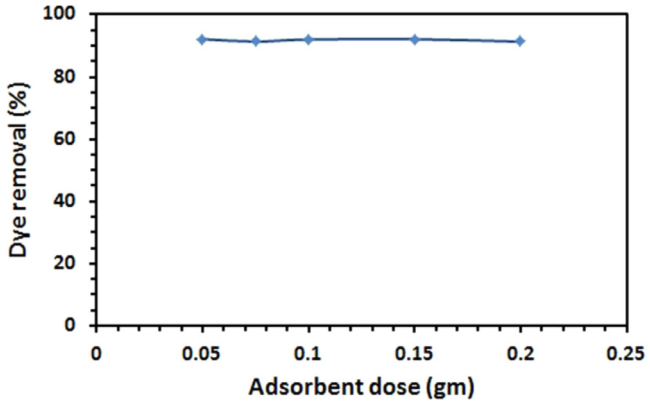

Fig. 8. Influence of adsorbent Mn_2O_3 dose on RB5 dye removal percentage.

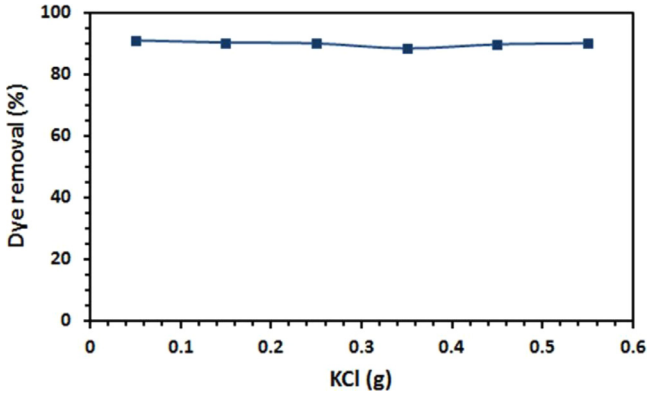

Fig. 9. Influence of ionic strength on RB5 dye removal percentage.

consistent with the reported ones [56]. Plus, the broadness of the peak appeared at 3357 cm^{-1} can be assigned to the contribution from the stretching vibration of NH_2 group of the adsorbed RB5 dye molecules. Additionally, RB5 dye molecule adsorption process results in a shift of the peaks that were due to Mn–O stretching vibrations (Fig 2b); 491, 560, and 633 cm^{-1}, to 478, 547, and 702 cm^{-1}, respectively (Fig. 2c), and also their intensities were enhanced.

3.2.1. Effect of initial pH

Initial pH of the solution has a crucial role in the adsorption experiments due to its influence on the binding sites of the adsorbent (Mn_2O_3 nanoparticles) and the adsorbate (RB5 dye). The influence of the initial pH of the solution on the adsorption ability of Mn_2O_3 microspheres for RB5 dye ($C_0 = 30$ mg/L, $\lambda_{max} = 596$ nm) within the pH range of 1–9 for 24 h has been studied and depicted in Fig. 6. As shown in Fig. 6, it can easily be observed that the dye removal efficiency reached its maximum at pH *ca.* 1.5 then decreased slowly until pH = 4. Afterwards, increasing the initial pH over 4, resulted in decreasing the dye removal efficiency sharply till pH = 7, and when pH > 7, the removal efficiency reached its minimum, and hence the other adsorption experiments were performed at pH 1.5. The results can be illustrated on the basis of electrostatic attraction because it is mainly affected by pH value of solutions since at pHs lower than pH_{pzc} of the Mn_2O_3 nanoparticles ($pH_{pzc} = 6.3$ for Mn_2O_3 nanoparticles), the Mn_2O_3 particles are positively charged which results in attraction between the oppositely charged nanoparticles and dye molecules (negatively charged molecules) producing higher adsorption. However, at pHs > pH_{pzc} the adsorption will be very low due to the electrostatic repulsion between the similar charges (*i.e.* negatively charged species of $Mn_2O_3$and RB5 dye).

3.2.2. Effect of initial dye concentration

At pH 1.5 and room temperature, the effect of initial RB5 dye concentration (10–50 mg/L) of the adsorption of RB5 dye was explored as shown in Fig. 7. As clear in Fig. 7, the higher removal efficiency (96.3%) was obtained for initial dye concentration of 10 mg/L then increasing the initial dye concentration resulted in lowering the dye removal efficiency till it reached 88.5% at initial RB5 dye concentration of 50 mg/L. These results may be due to the fact that at higher initial concentrations of the RB5 dye, the number of RB5 dye molecules is greater than the number of surface sites available for adsorption on the Mn_2O_3adsorbent.

3.2.3. Effect of adsorbent dosage

Effect of the sorbent dosage of the Mn_2O_3 nanoparticles on the adsorption of RB5 dye (initial concentration = 30 mg/L) was investigated at pH 1.5 by changing the adsorbent quantity from 50 to 200 mg. The obtained data are depicted in Fig. 8. It can be easily seen that, the removal efficiency percentage (91.7%) of RB5 dye has almost not been enhanced on increasing the adsorbent dosage from 50 mg to 200 mg. This can be attributed to the unavailability of more adsorption active sites afforded by the adsorbent, and both the adsorbent surface and RB5 dye solution concentration reached the equilibrium [57].

3.2.4. Ionic strength effect

Due to the competition that may occur between the dissolved inorganic ions and the dye molecules for the adsorption on the active sites of the adsorbent, studying the effect of the ionic strength on the adsorption process is a crucial point [58]. In this work,

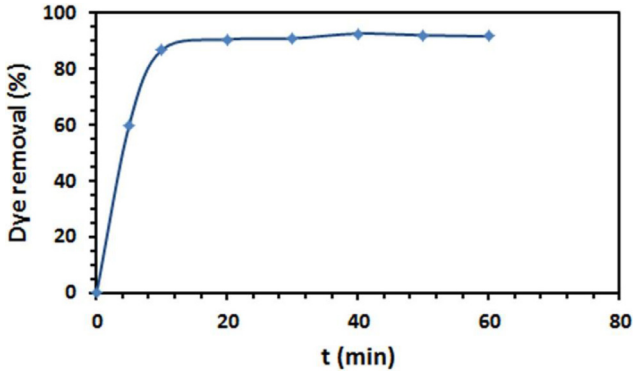

Fig. 10. Influence of contact time on RB5 dye removal percentage.

ionic strength influence on the adsorption process was investigated by using different concentrations of KCl salt (0.05–0.60 g), and the other parameters were set as 1.5 initial pH, 30 mg/L initial RB5 dye concentration (25 mL), room temperature, 40 min contact time, and 0.05 g adsorbent dose. The obtained data are presented in Fig. 9. The experimental results revealed that the removal efficiency percentage of the RB5 dye has not been affected by the presence of potassium chloride. Hence, interestingly, it can be concluded that this adsorption process can be exploited for removal of RB5 dye from wastewaters having high quantities of salts [59].

3.2.5. Kinetic studies

Because kinetics can provide valuable information about the rate at which the pollutant dye can be removed from aqueous solutions and can also help us understand the mechanism of the adsorption processes, kinetic studies are very essential in adsorption processes. The adsorption kinetic investigations were performed in a batch mode by studying the effect of contact time on the adsorption of RB5 dye at the optimum conditions: 1.5 initial pH, 0.05 g adsorbent, and 30 mg/L initial dye concentration, as given in Fig. 10. Fig. 10 exhibited that the adsorption capacity of the Mn_2O_3nanoparticles increased rapidly with time and reached its maximum ($q_e = 14.6$ mg/g) at 40 min and beyond this time it reached a plateau.

By fitting pseudo-first order equation [60], pseudo-second order equation [61], and intraparticle diffusion model [62] with the experimental results, one can get some information about the adsorbate quantity and the adsorption process rate through calculation of some kinetic parameters of RB5 dye adsorption on the Mn_2O_3adsorbent as presented in Fig 11. It is notable that the applicability of the kinetic model can be tested by investigating the linear regression value (*i.e.* correlation coefficient, r^2).

The linearized forms for the pseudo-first order and pseudo-second order models can be illustrated as in Eqs. (3) and (4), respectively.

$$\log (q_e - q_t) = \log q_e - \frac{k_1}{2.303} t \tag{3}$$

$$\frac{t}{q_t} = \frac{1}{k_2 q_e^2} + \frac{t}{q_e} \tag{4}$$

where, q_e (mg/g) is the equilibrium adsorption capacity, q_t (mg/g) is the adsorption capacity at time t (min), k_1 (1/min) is the pseudo-first order rate adsorption constant, and k_2 ((g/mg/min) is the rate constant of pseudo-second order rate adsorption constant. Moreover, using the plot of $\log(q_e - q_t)$ against t, k_1 values can be estimated. The obtained experimental results revealed that the pseudo-first order kinetic model (Fig. 11(a)) could not be used to describe the kinetics of the adsorption ($r^2 = 0.537$), and consequently pseudo-second order kinetic model had been tried and it

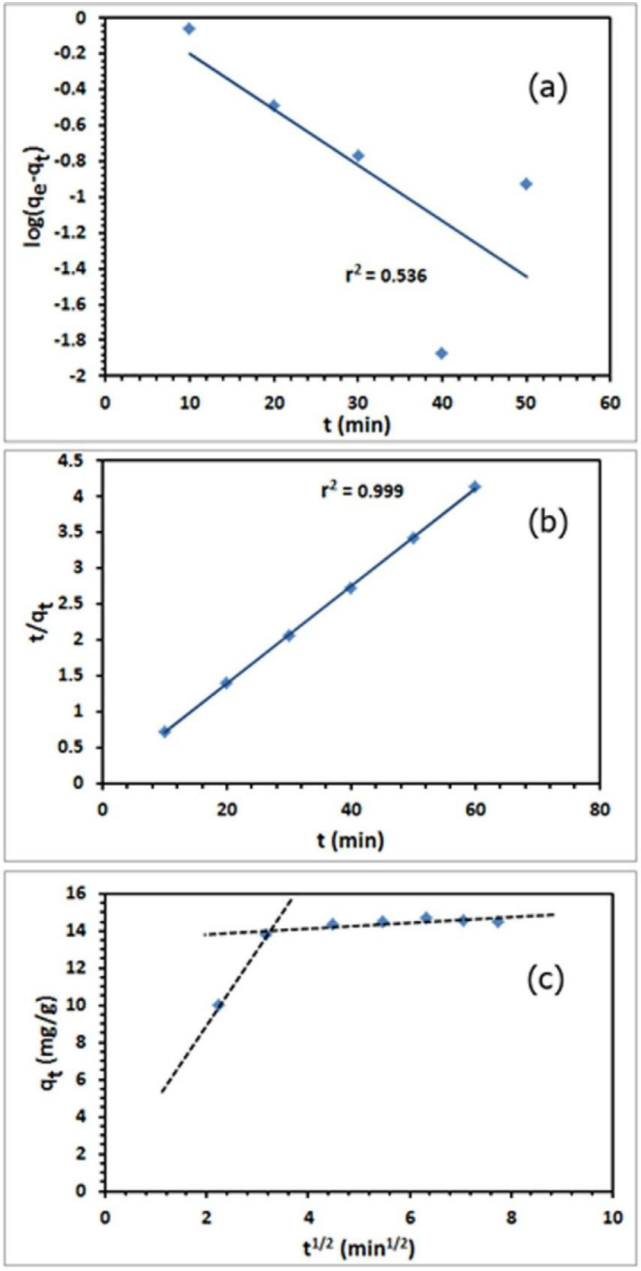

Fig. 11. (a–c). Pseudo-first-order (a), pseudo-second-order (b), and intra-particle diffusion model (c) for the adsorption of RB5 dye on Mn_2O_3 nanoparticles.

gave an excellent fitting ($r^2 = 0.999$). The pseudo-second order rate adsorption constant, k_2, was calculated using the t/q_t *versus* t plot, as given in Fig. 11(b). The experimental equilibrium adsorption capacity $q_{e(exp)}$, the calculated equilibrium adsorption capacity $q_{e(cal)}$, and some other adsorption kinetic constants for the adsorption of RB5 dye on Mn_2O_3 nanoparticles are given in Table 1. As previously mentioned, according to Fig. 11(a and b) and the regression coefficient values (Table 1), it can clearly be concluded that the adsorption of RB5 dye on Mn_2O_3nanoparticles can well be described by pseudo-second order model. Additionally, the calculated adsorption capacity value ($q_{e(cal)}$) is in good agreement with the experimental one ($q_{e(exp)}$). However, intra-particle diffusion model was tested by applying the Weber and Morris equation (Eq. 5) in order to evaluate the rate determining step for the adsorption of RB5 dye on Mn_2O_3 adsorbent.

$$q_t = k_i t^{0.5} + C \tag{5}$$

Table 1
Kinetic parameters for the adsorption of RB5 dye on Mn_2O_3 nanoparticles.

Kinetics models	Parameters	Value
Pseudo-first order	k_1 (1/min)	0.0716
	$q_{e(cal)}$ (mg/g)	1.29
	r_1^2	0.537
	$q_{e(exp)}$ (mg/g)	14.6
Pseudo-second order	k_2 (g/mg/min)	0.05
	$q_{e(cal)}$ (mg/g)	14.99
	r_2^2	0.999
	$q_{e,exp}$ (mg/g)	14.6

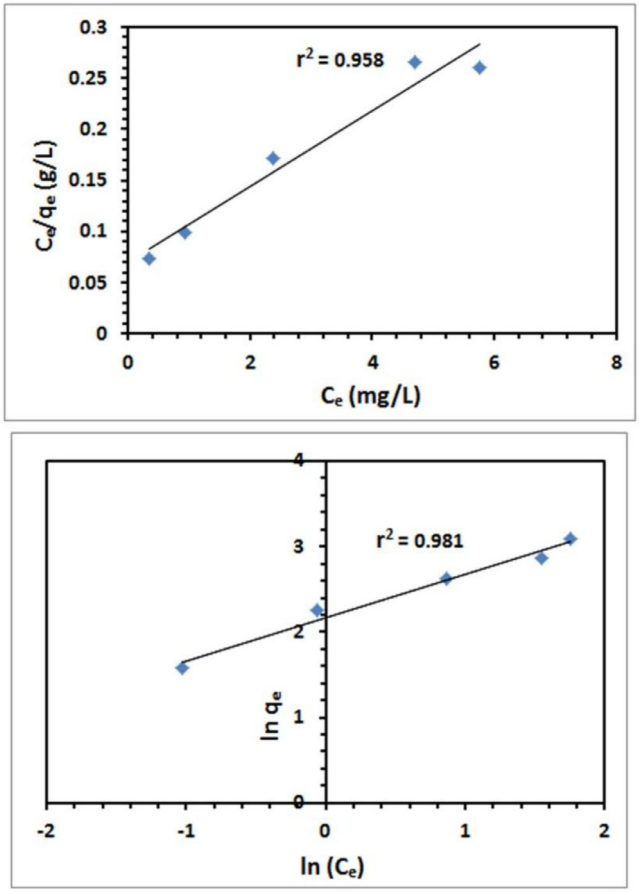

Fig. 12. (a,b). Langmuir isotherm (a), and Freundlich isotherm (b) plots for the adsorption of RB5 dye on Mn_2O_3 nanoparticles.

where k_i is the constant of intra-particle diffusion (mg/(g.min$^{1/2}$), and C is the intercept giving an idea about the boundary layer thickness (mg/g). The plot of q_t values *versus* $t^{0.5}$ values will be a straight line passing through the origin, if the rate determining step is the intra-particle diffusion only. Otherwise, the rate determining step will be a combination of intra-particle diffusion mechanism and others. In the present case, the plot of q_t *versus* $t^{0.5}$ as presented in Fig. 11c is a multilinear plot. It is also observed that the plot does not pass the origin and this indicates that the adsorption process is influenced and controlled by bulk diffusion, film diffusion, chemical reaction, and intra-particle diffusion mechanisms [63].

3.2.6. Adsorption isotherm modeling

Adsorption isotherms are the equilibrium relationships between the adsorbed quantity of the adsorbate (*i.e.* solid phase) on the adsorbent and its concentration in the solution (*i.e.* liquid phase).

Table 2
Isotherm constants for the adsorption of RB5 dye on Mn_2O_3 nanoparticles.

Isotherm models	Constants	Value
Langmuir	K_L (L/mg)	0.865
	$q_{m(cal)}$ (mg/g)	16.6
	r_1^2	0.958
	R_L	0.037
	$q_{e(exp)}$ (mg/g)	14.6
Freundlich	K_F [(mg/g)(L/mg)$^{1/n}$]	8.766
	$q_{m(cal)}$ (mg/g)	49.7
	r_2^2	0.981
	n	1.96
	$q_{e,exp}$ (mg/g)	14.6

In this work, at the optimal adsorption conditions, two well-known isotherms such as Langmuir and Freundlich models have been checked to fit the experimental adsorption results obtained through using different equilibrium concentrations of the RB5 dye. The linearized form of the Langmuir relation (Eq. 6) can be given as follows:

$$\frac{C_e}{q_e} = \frac{1}{K_L q_m} + \frac{C_e}{q_m} \tag{6}$$

where, C_e is the RB5 dye equilibrium concentration in solution (mg/L), q_e is the RB5 dye equilibrium adsorption capacity on the Mn_2O_3 adsorbent, K_L is the Langmuir adsorption constant (L/mg), and q_m is the maximum quantity of the adsorbed solute required to form a monolayer per gram of adsorbent (mg/g). The q_m and K_L constants can be estimated from the slope and intercept, respectively, of the linear plot of C_e/q_e against C_e (Fig. 12a). On the other hand, the linearized form of the Freundlich isotherm (Eq. 7) can be expressed as follows:

$$\ln q_e = \ln K_F + \frac{1}{n} \ln C_e \tag{7}$$

where, n and K_F are Freundlich constants representing the adsorption intensity and adsorption capacity, respectively, of the Mn_2O_3 adsorbent and they can be estimated using the intercept and slope of the linear plot of ln q_e *versus* ln C_e (Fig. 12b). The magnitude of the Freundlich constant, n, provides an indication on the favorability of adsorption. It is reported that if n falls in the range $2 < n < 10$, the adsorption is good; if n is in the range $1 < n < 2$, the adsorption is moderately difficult; and finally if $n < 1$, the adsorption is poor adsorption [64]. Conventionally, q_m (maximum adsorption capacity) can be calculated from the Langmuir model, as previously mentioned. However, this quantity can also be determined from the Freundlich model. Hence, to estimate the Freundlich maximum adsorption capacity, it is essential to work up with constant initial concentration (C_0) and varying adsorbent weights, and accordingly ln q_m is the extrapolated value of ln q for $C = C_0$ [65]. Thence, the Freundlich maximum adsorption capacity (q_m), according to Halsey [66], can be calculated using Eq. (8).

$$K_F = \frac{q_m}{C_0^{1/n}} \tag{8}$$

The regression coefficients and isotherm constants of the Langmuir and Freundlich plots are tabulated in Table 2. It is clear from this Table 2 that although both isotherms have similar values of correlation coefficient, the correlation coefficient (r^2) for the Freundlich model (0.981) is closer to unity than that for the Langmuir model (0.958). However, the expected maximum adsorption capacity $q_{m(cal)}$ value using the Freundlich model is much higher than the obtained experimental one which in the same time is closer to that calculated by applying the Langmuir isotherm. These results indicate that the experimental data fit well the Langmuir

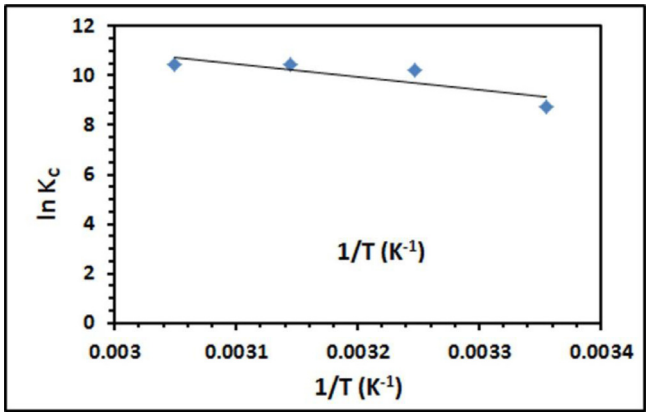

Fig. 13. Plot of ln K_c against $1/T$ for RB5 dye adsorption on Mn_2O_3 nanoparticles.

Table 3
Thermodynamic constants for adsorption of RB5 dye on Mn_2O_3 nanoparticles.

Temperature (K)	ln K_c	ΔG^0 (kJ/mol)	ΔH^0 (kJ/mol)	ΔS^0 (J/mol.K)
298	8.37	−21.63	44.52	0.225
308	10.20	−26.12		
318	10.43	−27.575		
328	10.45	−28.497		

model and this reveals the homogeneous nature of Mn_2O_3 surface. Based on this, it can be concluded that adsorption of the RB5 dye is monolayer coverage at the outer surface of Mn_2O_3 surface. Additionally, the efficiency of the adsorption of the RB5 dye on the adsorbent could be defined using the separation factor constant value (R_L) which was described in Eq. (9).

$$R_L = \frac{1}{1 + K_L C_o} \tag{9}$$

where K_L and C_0 are the Langmuir constant (L/mg), and initial concentration (mg/L), respectively. The value of the R_L shows whether the isotherm type is irreversible ($R_L = 0$), favorable ($0 < R_L < 1$), linear ($R_L = 1$), or unfavorable ($R_L > 1$). The calculated R_L value is estimated to be 0.037 which indicates that the adsorption of the RB5 dye on the Mn_2O_3 adsorbent is favorable at the optimal adsorption conditions.

3.2.7. Thermodynamic adsorption studies

Thermodynamic constants can give information about the energetic changes related to the adsorption process. As such, effect of the temperature of the media on the adsorption of RB5 dye on the Mn_2O_3adsorbent was studied at different temperatures; 298, 308, 318, and 328 K. The results revealed that increasing temperature from 298 to 328 K resulted in slightly increasing the adsorption capacity from 14.73 to 14.79 mg/g. Hence, it could be concluded that the adsorption of RB5 dye molecules on Mn_2O_3adsorbent was endothermic. Additionally, the thermodynamic constants including standard enthalpy (ΔH^0), standard entropy (ΔS^0), and standard Gibbs free energy (ΔG^0) can be determined by exploiting Eqs. (10)–(12).

$$\ln K_c = \frac{\Delta S^0}{R} - \frac{\Delta H^0}{RT} \tag{10}$$

$$\Delta G^0 = -RT \ln K_c \tag{11}$$

$$\Delta G^0 = \Delta H^0 - T\Delta S^0 \tag{12}$$

where K_c, R, and T are the thermodynamic equilibrium constant (L/g); $K_c = q_e/C_e$, universal gas constant (8.314 J/mol.K), and absolute solution temperature (K), respectively. According to Eq. (10), if ln K_c is plotted *versus* $1/T$, it will give a straight line (Fig. 13) and from the slope and intercept ΔS^0 and ΔH° can be estimated. Feeding these values in Eqs. 11 and 12, produces ΔG^0, and the values of the thermodynamic parameters are reported in Table 3. It is obvious from this table that adsorption of RB5 dye on the Mn_2O_3 nanoparticles is an endothermic process according to the obtained ΔH^0 positive value, and the process is spontaneous since the value of ΔG^0 is negative. Additionally, on increasing the temperature, the ΔG^0 values slightly decrease which means that the adsorption process of the RB5 dye Mn_2O_3 adsorbent is slightly more desirable at higher temperatures.

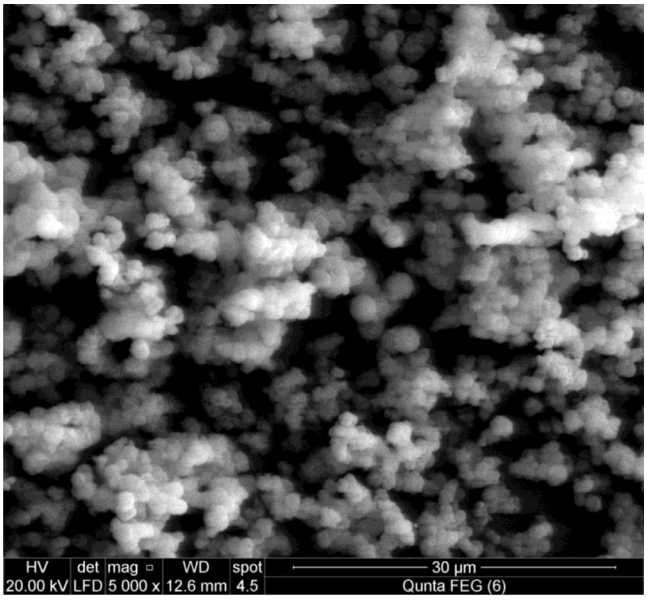

Fig. 14. FE-SEM image of RB5-loaded Mn_2O_3 adsorbent.

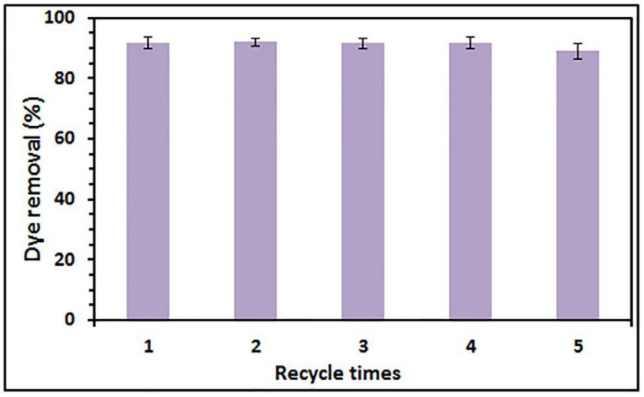

Fig. 15. Reusability of Mn_2O_3 adsorbent for RB5 dye adsorption.

3.2.8. Regeneration of Mn_2O_3 adsorbent

Regeneration of the adsorbent is very important for the reusability purpose for industrial applications. Fig. 14 depicts the FE-SEM image of the Mn_2O_3 adsorbent surface after adsorption process. It is clear that the dye molecules cover the Mn_2O_3 surface; since the surface of the RB5-loaded Mn_2O_3 is different from the surface of the pure Mn_2O_3 product especially appearance of the more darkened areas in the SEM image of the RB5-loaded Mn_2O_3. The as-prepared Mn_2O_3 adsorbent could be recovered with desorption ratio of 100% by first soaking the adsorbent in acetone for 4 h, washing with acetone and methanol, then drying at 60 °C for 3 h; using 0.01 M NaOH then washing with water and ethanol, and drying at 60 °C for 3 h; or alternatively by combustion the loaded

Table 4
Comparison of adsorption capacities of different adsorbents with Mn_2O_3 nanoparticles for RB5 dyes removal.

Adsorbents	Adsorption capacities, q_m (mg/g)	Refs.
Sunflower seed shells	1	[66]
Biomass fly ash	4.38	[67]
High lime Soma fly ash	7.18	[68]
Coal fly ash (high lime)	7.936	[69]
Cetyltrimethylammonium bromide modified zeolite	12.93	[70]
Mn_2O_3	14.6	This study
Modified zeolites	61	[71]
Modified clay (sepiolite)	120.5	[72]

Mn_2O_3 adsorbent at 500 °C for 30 min. The regenerated adsorbent could remove similar quantities of RB5 dye even after fifth regenerations, as shown in Fig. 15. As compared to the first adsorption, the dye removal efficiency percentage decreased from *ca.* 92% to 89% at the fifth cycle, giving an indication of good regeneration and reusability of the as-prepared Mn_2O_3 adsorbent, supporting the long term use of the adsorbent in water treatment.

3.2.9. Comparison with other adsorbents

Finally, a comparison of maximum adsorption capacity, q_m, on Mn_2O_3 nanoparticles with some other adsorbents for RB5 dye removal is listed in Table 4. It is clear that Mn_2O_3 adsorbent has relatively higher maximum adsorption capacity toward RB5 dye among most of the listed adsorbents. Though some adsorbents have higher adsorption capacity for RB5 dye removal, characteristics of the as-prepared Mn_2O_3 adsorbent such as its desorption ratio 100% and reusability for about five times, are still attractive and make this adsorbent applicable in wastewater treatment.

4. Conclusions

In the current work, pure $MnCO_3$ microspheres were successfully prepared in high yield by hydrothermal treatment of manganese chloride and ammonium hydrogen carbonate with molar ratio of 1:3, respectively, at 80 °C for 0.5 h. Afterwards, thermal decomposition of the as-prepared manganese carbonate at 550 °C for 1 h produced pure Mn_2O_3 nanoparticles. It is probable that this method can be generalized to prepare other metal oxides in pure form. The as-prepared Mn_2O_3 nanoparticles showed good adsorption properties toward Reactive Black 5 (RB5) dye and hence manganese oxide nanoparticles can be used to purify wastewater from this dye. The adsorption data fitted very well with the Langmuir isotherm model indicating that the adsorption process was essentially monolayer coverage. The spontaneous and endothermic natures of the adsorption process were confirmed form the thermodynamic studies.

Acknowledgment

The authors thank Benha University, Egypt, for the financial support of the current research work.

References

[1] Khan TA, Chaudhry SA, Ali I. Equilibrium uptake, isotherm and kinetic studies of Cd(II) adsorption onto iron oxide activated red mud from aqueous solution. J Mol Liq 2015;202:165–75.
[2] Khan TA, Nazir M, Ali I, Kumar A. Removal of chromium(VI) from aqueous solution using guar gum–nano zinc oxide biocomposite adsorbent. Arab J Chem 2013. doi:10.1016/j.arabjc.2013.08.019.
[3] Nassar MY, Ahmed IS, Mohamed TY, Khatab M. A controlled, template-free, and hydrothermal synthesis route to sphere-like α-Fe2O_3 nanostructures for textile dye removal. RSC Adv 2016;6:20001–13.
[4] Khan TA, Singh VV. Removal of cadmium(II), lead(II), and chromium(VI) ions from aqueous solution using clay. Toxicol Environ Chem 2010;92:1435–46.
[5] Khan TA, Singh VV, Ali I. Sorption of Cd(II), Pb(II), and Cr(VI) metal ions from wastewater using bottom fly ash as a low cost sorbent. J Environ Protect Sci 2009;3:124–32.
[6] Qadri S, Ganoe A, Haik Y. Removal and recovery of acridine orange from solutions by use of magnetic nanoparticles. J Hazard Mater 2009;169(1-3):318–323.
[7] Venkatesha TG, Viswanatha R, Nayaka YA, Chethana BK. Kinetics and thermodynamics of reactive and vat dyes adsorption on MgO nanoparticles. Chem Eng J 2012;198-199:1–10.
[8] Tanhaei B, Ayati A, Lahtinen M, Sillanpaa M. Preparation and characterization of a novel chitosan/Al_2O_3/magnetite nanoparticles composite adsorbent for kinetic, thermodynamic and isotherm studies of methyl orange adsorption. Chem Eng J 2015;259:1–10.
[9] Nematollahzadeh A, Shojaei A, Karimi M. Chemically modified organic/inorganic nanoporous composite particles for the adsorption of Reactive Black 5 from aqueous solution. React Funct Polym 2015;86:7–15.
[10] Ballav N, Debnath S, Pillay K, Maity A. Efficient removal of Reactive Black from aqueous solution using polyaniline coated ligno-cellulose composite as a potential adsorbent. J Mol Liq 2015;209:387–96.
[11] Das SK, Bhowal J, Das AR, Guha AK. Adsorption behavior of rhodamine B on rhizopus o ryzae biomass. Langmuir 2006;22:7265–72.
[12] Khan TA, Nazir M, Khan EA. Adsorptive removal of rhodamine B from textile wastewater using water chestnut (Trapa natans L.) peel: adsorption dynamics and kinetic studies. Toxicol Environ Chem 2013;95:919–31.
[13] Nassar MY, Ahmed IS. A novel synthetic route for magnesium aluminate ($MgAl_2O_4$) nanoparticles using sol-gel auto combustion method and their photocatalytic properties. Spectrochim Acta part A 2014;131:320–34.
[14] Yang C, Zhua Y, Wanga J, Lia Z, Sua X, Niu C. Hydrothermal synthesis of TiO_2–WO_3–bentonite composites: conventional versus ultrasonic pretreatments and their adsorption of methylene blue. Appl Clay Sci 2015;105–106:243–51.
[15] Tanhaei B, Ayati A, Lahtinen M, Sillanpaa M. Preparation and characterization of a novel chitosan/Al_2O_3/magnetite nanoparticles composite adsorbent for kinetic, thermodynamic and isotherm studies of methyl orange adsorption. Chem Eng J 2015;259:1–10.
[16] Bhattacharyya R, Ray SK. Micro- and nano-sized bentonite filled composite superabsorbents of chitosan and acrylic copolymer for removal of synthetic dyes from water. Appl Clay Sci 2014;101:510–20.
[17] Nassar MY, Ahmed IS. Template-free hydrothermal derived cobalt oxide nanopowders: synthesis, characterization, and removal of organic dyes. Mater Res Bull 2012;47:2638–45.
[18] Khan TA, Khan EA, Shahjahan EA. Removal of basic dyes from aqueous solution by adsorption onto binary iron-manganese oxide coated kaolinite: non-linear isotherm and kinetics modeling. Appl Clay Sci 2015;107:70–7.
[19] Hameed BH. Equilibrium and kinetics studies of 2,4,6-trichlorophenol adsorption onto activated clay. Colloid Surface A 2007;307:45–52.
[20] Cornelissen ER, Moreau N, Siegers WG, Abrahamse AJ, Rietveld LC, Grete A, et al. Selection of anionic exchange resins for removal of natural organic matter (NOM) fractions. Water Res 2008;42:413–23.
[21] Feng Y, Yang F, Wang Y, Ma L, Wu Y, Kerr PG, et al. Basic dye adsorption onto an agro-based waste material-Sesame hull (Sesame indicum L.). Bioresour Technol 2011;102:10280–5.
[22] Xu R-K, Xiao S-C, Yuan J-H, Zhao A-Z. Adsorption of methyl violet from aqueous solutions by the biochars derived from crop residues. Bioresour Technol 2011;102:10293–8.
[23] Nassar MY, Ahmed IS. Hydrothermal synthesis of cobalt carbonates using different counter ions: an efficient precursor to nano-sized cobalt oxide (Co_3O_4). Polyhedron 2011;30:2431–7.
[24] Wang E, Hu L, Lei S, Zhang S, Zhang S, Gong W. Influence of calcination atmosphere on adsorptive performance of composite minerals materials. Appl Clay Sci 2015;118:138–50.
[25] Jiao T, Liu Y, Wu Y, Zhang Q, Yan X, Gao F, et al. Facile and scalable preparation of graphene oxide-based magnetic hybrids for fast and highly efficient removal of organic dyes. Sci Rep 2015;5:12451.
[26] Guo H, Jiao T, Zhang Q, Guo W, Peng Q, Yan X. Preparation of graphene oxide-based hydrogels as efficient dye adsorbents for wastewater treatment. Nanoscale Res Lett 2015;10:272.
[27] Luo C, Tian Z, Yang B, Zhang L, Yan S. Manganese dioxide/iron oxide/acid oxidized multi-walled carbon nanotube magnetic nanocomposite for enhanced hexavalent chromium removal. Chem Eng J 2013;234:256–65.
[28] Wang W, Jiao T, Zhang Q, Luo X, Hu J, Chen Y, et al. Hydrothermal synthesis of hierarchical core-shell manganese oxide nanocomposites as efficient dye adsorbents for wastewater treatment. RSC Adv 2015;5:56279–85.
[29] Abdel Salam M. Synthesis and characterization of novel manganese oxide nanocorals and their application for the removal of methylene blue from aqueous solution. Chem Eng J 2015;270:50–7.
[30] Ge X, Gu CD, Wang XL, Tu JP. Endowing manganese oxide with fast adsorption ability through controlling the manganese carbonate precursor assembled in ionic liquid. J Colloid Interf Sci 2015;438:149–58.
[31] Wu HB, Chen JS, Hng HH, Lou XWD. Nanostructured metal oxide-based materials as advanced anodes for lithium-ion batteries. Nanoscale 2012;4:2526–2542.

[32] Seo WS, Jo HH, Lee K, Kim B, Oh SJ, Park JT. Size-dependent magnetic properties of colloidal Mn_3O_4 and MnO nanoparticles. Angew Chem Int Ed 2004;43:1115–17.
[33] Gnanam S, Rajendran V. Novel morphologies, sizes, optical and antibacterial activity of organic acids assisted manganese sesquioxide (α-Mn_2O_3) nanostructures via precipitation route. J Alloy Compd 2014;617:975–8.
[34] Gnanam S, Rajendran V. Synthesis of CeO_2 or α-Mn_2O_3 nanoparticles via sol-gel process and their optical properties. J Sol Gel Sci Technol 2011;58:62–69.
[35] Ren Y, Liu Q, Wang J, Wang H, Xue D. Large-scale synthesis of single-crystal alpha manganese sesquioxide nanowires via solid-state reaction. Mater Lett 2009;63:661–3.
[36] Gnanam S, Rajendran V. Facile hydrothermal synthesis of alpha manganese sesquioxide (α-Mn_2O_3) nanodumb-bells: structural, magnetic, optical and photocatalytic properties. J Alloy Compd 2013;550:463–70.
[37] Salavati-Niasari M, Esmaeili-Zare M, Gholami-Daghian M. Synthesis and characterization of Mn_2O_3 nanorods using a novel manganese precursor. Adv Powder Technol 2014;25:879–84.
[38] Yuan ZY, Zhang ZL, Du GH, Ren TZ, Su BL. A simple method to synthesise signle-crystalline manganese oxide nanowires. Chem Phys Lett 2003;378:349–53.
[39] Esmaeili-Zare M, Salavati-Niasari M, Sobhani A. Simple sonochemical synthesis and characterization of HgSe nanoparticles. Ultrason Sonochem 2012;19:1079–86.
[40] Liang H, Meng F, Cabán-Acevedo M, Li L, Forticaux A, Xiu L, et al. Hydrothermal continuous flow synthesis and exfoliation of NiCo layered double hydroxide nanosheets for enhanced oxygen evolution catalysis. Nano Lett 2015;15:1421–7.
[41] Nassar MY, Mohamed TY, Ahmed IS. One-pot solvothermal synthesis of novel cobalt salicylaldimine-urea complexes: a new approach to Co_3O_4 nanoparticles. J Mol Struct 2013;1050:81–7.
[42] Kaneko K, Inoke K, Freitag B, Hungria AB, Midgley PA, Hansen TW, et al. Structural and morphological characterization of cerium oxide nanocrystals prepared by hydrothermal synthesis. Nano Lett 2007;7:421–5.
[43] Nassar MY. Size-controlled synthesis of $CoCO_3$ and Co_3O_4 nanoparticles by free-surfactant hydrothermal method. Mater Lett 2013;94:112–15.
[44] Yang T, Huang Z, Liu Y, Fang M, Ouyang X, Hu M. Controlled synthesis of porous $FeCO_3$ microspheres and the conversion to α-Fe_2O_3 with unconventional morphology. Ceram Int 2014;40:11975–83.
[45] Peng J, Feng L-N, Zhang K, Li J-J, Jiang L-P, Zhu J-J. Multifunctional manganese carbonate microspheres with superparamagnetic and fluorescent properties: synthesis and biological application. Chem Eur J 2011;17:10916–23.
[46] Tong W, Gao C. Selective removal of particle cores to fabricate manganese carbonate hollow spheres and composite microcapsules. Colloid Surface A 2007;295:233–8.
[47] Jenkins R, Snyder RL. Chemical analysis: introduction to X-ray powder diffractometry. New York: John Wiley and Sons, Inc.; 1996.
[48] Lee JH, Sa YJ, Kim TK, Moon HR, Joo SH. A transformative route to nanoporous manganese oxides of controlled oxidation states with identical textural properties. J Mater Chem A 2014;2:10435–43.
[49] Nakamoto K. Infrared and Raman spectra of inorganic and coordination compounds. Pt. B: Applications in coordination, organometallic, and bioinorganic chemistry. 5th ed. New York: Wiley-Interscience; 1997.
[50] Sekhar BC, Babu G, Kalaiselvi N. Nanoflake driven Mn_2O_3 microcubes modified with cooked rice derived carbon for improved electrochemical behavior. RSC Adv 2015;5:4568–77.
[51] Nassar MY, Attia AS, Alfallous KA, El-Shahat MF. Synthesis of two novel dinuclear molybdenum(0) complexes of quinoxaline-2,3-dione: New precursors for preparation of α-MoO_3 nanoplates, Inorg. Chim Acta 2013;405:362–7.
[52] Han Y-F, Chen L, Ramesh K, Zhong Z, Chen F, Chin J, et al. Coral-like nanostructured α-Mn_2O_3 nanaocrystals for catalytic combustion of methane Part I. Prep Charact Catal Today 2008;131:35–41.
[53] Jacob KT, Kumar A, Rajitha G, Waseda Y. Thermodynamic data for Mn_3O_4, Mn_2O_3 and MnO_2. High Temp Mater Proc 2011;30:459–72.
[54] Liu R, Zhao S, Zhang M, Feng F, Shen Q. High interfacial lithium storage capability of hollow porous Mn_2O_3 nanostructures obtained from carbonate precursors. Chem Commun 2015;51:5728–31.
[55] Kim MH, Hwang C-H, Kang SB, Kim S, Park SW, Yun Y-S, et al. Removal of hydrolyzed Reactive Black 5 from aqueous solution using a polyethylenimine–polyvinyl chloride composite fiber. Chem Eng J 2015;280:18–25.
[56] Naiya TK, Bhattacharya AK, Das SK. Adsorption of Cd(II) and Pb(II) from aqueous solutions on activated alumina. J Colloid Interface Sci 2009;333:14–26.
[57] Mahmoodi NM, Najafi F. Preparation of surface modified zinc oxide nanoparticle with high capacity dye removal ability. Mater Res Bull 2012;47:1800–1809.
[58] Chern JM, Wu CY. Desorption of dye from activated carbon beds: effects of temperature, pH and alcohol. Water Res 2001;35:4159–65.
[59] Sepehr MN, Sivasankar V, Zarrabi M, Kumar MS. Surface modification of pumice enhancing its fluoride adsorption capacity: an insight into kinetic and thermodynamic studies. Chem Eng J 2013;228:192–204.
[60] Ho YS, McKay G. Pseudo-second order model for sorption processes. Process Biochem 1999;34:451–65.
[61] Weber Jr WJ, Morris JC. Kinetics of adsorption on carbon from solution. J Sanitary Div Eng, Proc Am Soc Civ Eng 1963;89:31–59.
[62] Luo C, Tian Z, Yang B, Zhang L, Yan S. Manganese dioxide/iron oxide/acid oxidized multi-walled carbon nanotube magnetic nanocomposite for enhanced hexavalent chromium removal. Chem Eng J 2013;234:256–65.
[63] Treybal RE. Mass-transfer operations. 3rd ed. New York: McGraw-Hill; 1981.
[64] Djeribi R, Hamdaoui O. Sorption of copper (II) from aqueous solutions by cedar sawdust and crushed brick. Desalination 2008;225:95–112.
[65] Halsey G. The role of surface heterogeneity in adsorption. Adv Catal 1952;4:259–69.
[66] Osma JF, Saravia V, Toca-Herrera JL, Couto SR. Sunflower seed shells: a novel and effective low-cost adsorbent for the removal of the diazo dye Reactive Black 5 from aqueous solutions. J Hazard Mater 2007;147:900–5.
[67] Pengthamkeerati P, Satapanajaru T, Singchan O. Sorption of reactive dye from aqueous solution on biomass fly ash. J Hazard Mater 2008;153:1149–56.
[68] Eren Z, Acar FN. Equilibrium and kinetic mechanism for Reactive Black 5 sorption onto high lime Soma fly ash. J Hazard Mater 2007;143:226–32.
[69] Eren Z, Acar FN. Adsorption of Reactive Black 5 from an aqueous solution: equilibrium and kinetic studies. Desalination 2006;194:1–10.
[70] Karadag D, Turan M, Akgul E, Tok S, Faki A. Adsorption equilibrium and kinetics of Reactive Black 5 and Reactive Red 239 in aqueous solution onto surfactant-modified zeolite. J Chem Eng Data 2007;52:1615–20.
[71] Armağan B, Özdemir O, Turan M, Çelik MS. The removal of reactive azo dyes by natural and modified zeolites. J Chem Technol Biot 2003;78:725–32.
[72] Ozdemir O, Armagan B, Turan M, Celik MS. Comparison of the adsorption characteristics of azo-reactive dyes on mezoporous minerals. Dyes Pigm 2004;62:49–60.